Homogenisation method based on energy conservation and independent of boundary conditions

Zwarts, Sijmen; Lesueur, Martin

DOI
10.1016/j.advwatres.2023.104603

Publication date
2023

Document Version
Final published version

Published in
Advances in Water Resources

Advances in Water Resources 183 (2024) 104603

Contents lists available at ScienceDirect

Advances in Water Resources

journal homepage: www.elsevier.com/locate/advwatres

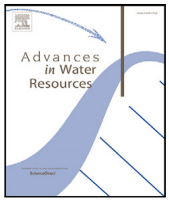

Homogenisation method based on energy conservation and independent of boundary conditions

Sijmen Zwarts *, Martin Lesueur

Civil Engineering and Geosciences, Delft University of Technology, Delft, The Netherlands

ARTICLE INFO

Keywords:
Homogenisation
Energy conservation
Representative elementary volume

ABSTRACT

The foundation of homogenisation methods rests on the postulate of Hill–Mandel, describing energy consistency throughout the transition of scales. The consideration of this principle is therefore crucial in the discipline of Digital Rock Physics which focuses on the upscaling of rock properties. For this reason, numerous studies have developed numerical schemes for porous media to enforce the Hill–Mandel condition to be respected. The most common method is to impose specific boundary conditions, such as periodic ones. However, these boundary conditions influence both the effective property and the size of the REV. The recent study of Thovert and Mourzenko (2020) has shown that most boundary conditions still result in the same intrinsic effective physical property if the averaging is applied outside the range of the boundary layer. From this discovery, it becomes logical to question the status of Hill–Mandel postulate in porous media when homogenising away from the boundary. In this contribution, we simulate Stokes flow through random packings of spheres and a range of rock microstructures. For each, we plot the evolution of the ratio micro- vs macro-scale of the energy of the fluid transport outside the boundary layer, for a growing subsample size of porous media. Here, we prove that we naturally find energy consistency across scales when reaching the size of the Representative Elementary Volume (REV), which is a known condition for rigorous upscaling. Furthermore, we show that this index for the energy consistency is a more accurate indicator of REV convergence since the mean value is already known to be unitary.

1. Introduction

In an attempt to reduce and replace destructive experiments, the goal of Digital Rock Physics (DRP) is to determine the physical response of the rock at the macro-scale, using simulations on the digitised microstructure. It is widely acknowledged that physical rock properties are mainly determined by the geometry and arrangement of grains at the microscale, under the concept of structure–property relationships. For example, rock permeability, which is the focus of this contribution, has been shown to be influenced by the grain shape (Beard and Weyl, 1973). The characterisation of permeability has later been extended to more morphological parameters of the rock microstructure (Cox and Budhu, 2008; Torskaya et al., 2014). Given the existence of scale separation between the microscopic level, obtained with μCT-imaging, and the macro-scale, rock properties can be obtained through homogenisation (Auriault, 2011).

The foundation of homogenisation methods rests on the Hill–Mandel (Hill, 1963; Mandel, 1972) principle, which states that energy cannot be created or destroyed in a closed system and thus remains consistent. In the context of homogenisation schemes, the principle is applied by conserving energy throughout the transition of scales, which means that the energy of the different scales should be identical to be able to apply homogenisation from the lower scale. As the local energy inside the heterogeneous microstructure can spatially vary significantly, usual homogenisation procedures apply the variation principle and split the energy into an average and fluctuation term. Only when the fluctuation of the energy becomes zero does the homogenised energy of the micro-scale have achieved consistency across the scales. To make sure that the fluctuation of the energy is zero, current homogenisation schemes impose specific types of boundary conditions. For the homogenisation of permeability, which is a hydraulic property, we are looking at the work energy of the fluid transport. It is shown that this energy consistency is enforced by applying kinematic, traction or periodic boundary conditions (Bøe, 1994; Renard and de Marsily, 1997; Du and Ostoja-Starzewski, 2006; Su et al., 2011; Marinelli et al., 2016; Paéz-García et al., 2017; Khoei et al., 2023). However, those different boundary conditions significantly influence the effective permeability of the rock sample. By imposing either a pressure gradient or a constant flux boundary condition at the inlet/outlet, the permeability becomes

* Corresponding author.
E-mail address: s.zwarts@tudelft.nl (S. Zwarts).

https://doi.org/10.1016/j.advwatres.2023.104603
Received 7 August 2023; Received in revised form 5 December 2023; Accepted 6 December 2023
Available online 11 December 2023

respectively maximal and minimal (Pouya and Fouche, 2009). Similar effects are shown by applying closed walls, periodic flows, slip or pressure external boundary conditions, as the permeability is influenced in both direction and magnitude (Andrae et al., 2013; Guibert et al., 2015; Gerke et al., 2019; Shi et al., 2020; Zakirov and Khramchenkov, 2022). These effects can also be seen when mechanical behaviour is included, shown in the frameworks of Nguyen et al. (2012), Jänicke et al. (2015), Sandström et al. (2016), Khoei and Hajiabadi (2018), Saeedmonir and Khoei (2022) and Khoei et al. (2023), which present different behaviour between linear or periodic boundary conditions.

To overcome this homogenisation challenge, we refer back to the foundational paper of Hill (1963), who states that the fluctuation of the mean becomes insignificant within a few wavelengths of the surface and the contribution of the surface layer becomes negligible by taking the sample large enough. This means that upon increasing the sample size, away from the boundary, the homogenised property will converge to the effective property, despite the different boundary conditions. Note that the size where convergence is reached is called the Representative Elementary Volume (REV), which can be used to create a homogeneous equivalent medium for the larger scale. However, depending on the type of external boundary conditions, the size of the REV can vary. In the case of Dirichlet or Neumann boundary conditions, they converge when REV is reached but periodic boundary condition has been shown to converge to REV earlier (Terada et al., 2000; Kanit et al., 2003; Larsson et al., 2011). An influence of the boundary conditions on either the REV value or size is unacceptable because, in essence, the REV is an intrinsic property of the porous material and should therefore be independent of numerical artefacts.

Instead, Hill's concept of attenuating fluctuation away from the boundary has recently been illustrated by Thovert and Mourzenko (2020), which studied the influence of the boundary conditions when determining the transport coefficients of a sample. The study shows that the effective permeability of an intrinsic sub-volume, away from the boundary, appears to be identical, despite considering different boundary conditions. However, when the boundary layer is taken into account, the permeability will vary depending on the different boundary conditions implemented. For example, the mean permeability can be up to ten times higher than the effective property when Dirichlet boundary conditions are applied to all the external boundaries. Therefore, it was recommended to compute the effective permeability inside an intrinsic volume, away from the boundary layer, such that the boundary does not influence the homogenised property. This is already applied in our recent work (Lesueur et al., 2022a).

Due to the influence of the boundary condition on the effective property and the size of the REV, it becomes logical to question the purpose of the boundary conditions currently deemed necessary for homogenisation schemes to enforce energy consistency throughout scales, as mentioned previously. When it comes to the Hill–Mandel principle, indeed, we expect the energy dissipation of the fluid transport to be influenced in a similar way to the fluid flow by the boundary conditions. Therefore, we wonder what becomes of the energy consistency across the scales in the intrinsic volume, away from the boundary. Is the Hill–Mandel principle still respected away from the boundary layer, unaffected by the boundary conditions? In this contribution, we devise a method to trace the evolution of the energy dissipation of fluids in the sample during a REV convergence. The method is then put to test on both idealised porous media and real microstructures, to verify if the results found are affected by natural heterogeneities.

2. Material and methods

2.1. Flow model

Assuming incompressible fluids, the lack of body forces, the lack of inertial effects and stationary solutions, which is the most common environment for fluid transport in the subsurface, one will automatically arrive at Stokes flow. The momentum and mass balance of the fluid implemented for the flow simulations are expressed as

$$\mu\nabla^2\boldsymbol{v} - \boldsymbol{\nabla}p = 0, \tag{1}$$

$$\nabla\cdot\boldsymbol{v} = 0, \tag{2}$$

with $\boldsymbol{v}$ the fluid velocity, p the pore pressure and μ the viscosity. Note that the bold characters indicate vectors and the non-bold characters are scalars. MOOSE (Permann et al., 2020; Peterson et al., 2018) is used to implement the Stokes flow equations, following the framework of Lesueur et al. (2017). We impose a normalised unitary viscosity for each sample. The classical no-slip (the velocity of the fluid is equal to zero in all directions) condition is applied on the boundary of the grains inside the sample, which relates to non-penetrable grains. The external boundary conditions to impose the flow and to solve the simulation are discussed in more detail in Section 2.5. An example of the flow through a cross-section of a random packing is shown in Fig. 1.

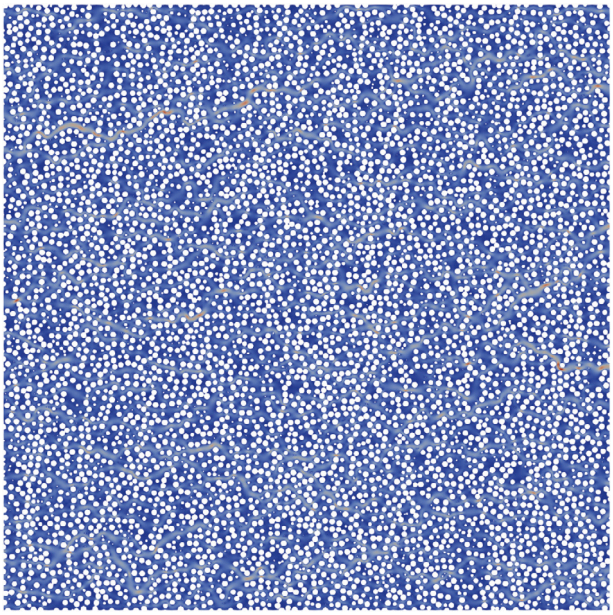

Fig. 1. Example of flow through a random packing of spheres. The figure visualises a cross-section, with a porosity of 53% of spheres of 0.005 diameter (compared to a total volume of 1). The grains are shown as white disks and the velocity of the fluid is shown in the coloured range, where blue is low velocity and red is high velocity.

2.2. Permeability homogenisation

We also compute the permeability, since the energy consistency of the fluid flow is a prerequisite of the latter. The permeability is postprocessed using Darcy's law (Darcy, 1856), which describes the relationship of Darcy's flux (q) with the permeability (k_{ii}) of a porous medium in the direction ($i = x, y, z$) of the flow. Darcy's flux is directly related to the average of Stokes flow-velocity of the fluid through the grains ($\overline{v_i}$) by multiplying the velocity with the porosity (φ) of the microstructure. This results in the following formulation of the permeability specifically expressed in index notation here as:

$$k_{ii} = \varphi\overline{v_i}\mu/\overline{\nabla p_i}. \tag{3}$$

Note that the overhead bar is used to indicate an average value, which is computed as:

$$\overline{X} = \frac{1}{V}\int_V X\,dV. \tag{4}$$

Darcy's law was initially formulated based on the results of experiments and has later been verified to be a homogenisation of the Stokes

formulation (Whitaker, 1986). The pressure gradient is either imposed due to the boundary conditions or can be found by averaging and similar for the velocity.

2.3. Energy consistency index

Hill–Mandel principle of energy consistency across scales can be expressed physically as the equality between the macro-scale energy dissipation and the homogenised micro-scale energy dissipation, thereby referred to as upscaled energy. For our system where the energy dissipation of the fluid transport is calculated by taking the product of the pressure gradient and the velocity of the fluid, the principle states that:

$$\overline{\nabla p} \cdot \overline{\boldsymbol{v}} = \overline{\nabla p \cdot \boldsymbol{v}}, \tag{5}$$

in which the pressure gradient and the velocity are both vectors, denoted in bold. Note that the energy dissipation was confirmed to be mathematically related to the permeability (Du and Ostoja-Starzewski, 2006). The local velocity of the fluid and pressure gradient can be expressed in terms of the average value (indicated with the overhead line) and the fluctuation (indicated with the overhead tilde) (Whitaker, 1986; Du and Ostoja-Starzewski, 2006):

$$\nabla p = \overline{\nabla p} + \widetilde{\nabla p}, \tag{6}$$

$$\boldsymbol{v} = \overline{\boldsymbol{v}} + \widetilde{\boldsymbol{v}}. \tag{7}$$

The average of the local energy dissipation, therefore, becomes:

$$\overline{\nabla p \cdot \boldsymbol{v}} = \overline{\nabla p} \cdot \overline{\boldsymbol{v}} + \overline{\widetilde{\nabla p} \cdot \widetilde{\boldsymbol{v}}}. \tag{8}$$

This equation shows that Hill–Mandel principle is respected when the energy dissipation from the microscale becomes stable, i.e. the fluctuations average out. Traditionally, Dirichlet and Neumann boundary conditions are implemented to nullify fluctuations at the boundary which allows to implement rigorous homogenisation. Periodic conditions have also been shown to have the same effect. In this contribution, in order to determine whether a sample has reached energy consistency and how far it is from it, we define an energy consistency index i_{HM} as the ratio between the energy of the two scales:

$$i_{HM} = \frac{\overline{\nabla p} \cdot \overline{\boldsymbol{v}}}{\overline{\nabla p \cdot \boldsymbol{v}}}. \tag{9}$$

This index is conveniently chosen to be unitary once energy consistency is achieved.

2.4. REV convergence

Tracing the evolution of an effective property during a REV convergence is usually done by running multiple simulations on samples of increasing size. Every point on the curve corresponds to the effective property of one sample at full size. This is plotted in Fig. 2 with every black cross (postprocessed away from the boundary layer). In this contribution instead, we only consider intrinsic subsamples, where the effective property is postprocessed away from the boundary layer in order to recover the natural conditions of fluid flow. Thovert and Mourzenko (2020) does not prescribe how far away should we be from the boundary layer. We speculate that his results are still correct independently of the size of the subsample if we are away from the boundary layer. To verify this approach, we conduct flow simulations, applying external classical no-slip boundary conditions and pressure-induced flow conditions at the inlet/outlet, to subsamples of the same random packing with growing in size (with a stepsize of 5% in linear length), growing from the middle of the random packing. For each, the energy dissipation is computed on a continuously growing postprocessing window which is captured on that specific subsample. The energy dissipation is normalised with respect to the value of the full-sized sample. The results are represented by each solid line in Fig. 2 and can

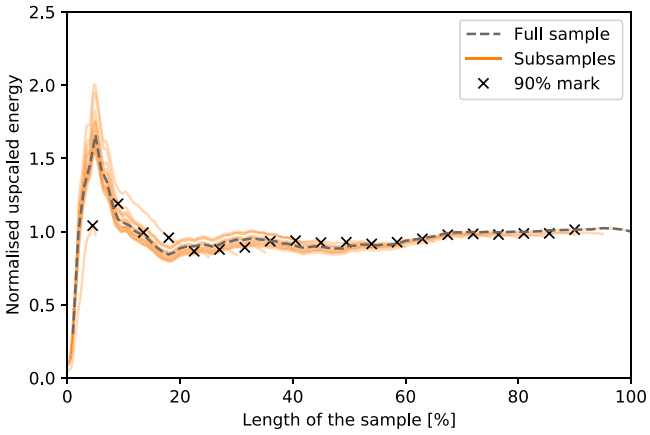

Fig. 2. The upscaled energy of a random packing with a porosity of 53% (normalised by the final value of the full random packing). Increasingly larger subsamples, growing from the centre of the sample, are used in the simulation, with a stepsize of 5% in size, from 5% up to 100% of the total random packing size. For each subsample the normalised energy is traced, starting from the centre. The black crosses indicate the upscaled energy for each subsample, postprocessed at 90% of the subsample size.

be compared to the discrete crosses obtained from the full subsamples. Note that the method to generate a random packing is described in more detail in Section 3.

We observe that the energy dissipation of the different sample sizes evolves in a nearly identical matter, following the same values and trend. This confirms that it is possible to compute and trace the effective property, with a single simulation by homogenising the property over a growing sub-sample within. However, when each subsample reaches its maximum size, we notice that the evolution of the energy dissipation diverges downwards from the previously stabilised value. For smaller subsamples, this effect is even stronger. This divergence can be explained by the influence of the boundary conditions that we characterise in the next subsection.

2.5. Boundary effects

The extent of the boundary layer needs to be determined so that the boundary conditions do not influence the computation of the effective properties. To achieve this, we test different model setups, by applying different boundary conditions. Specifically, two different flow conditions are considered. One imposes a normalised pressure gradient on the model, with a normalised pressure value of one at the inlet and zero at the outlet. The other model imposes an equal discharge at the inlet and the outlet, i.e. an average velocity such that the postprocessed average pressure gradient of this model is also (close to) one. In parallel, we consider slip (the velocity in the direction of the flow is set to zero, while the velocity in the normal direction is free), no-slip (the velocity components are both set to zero), or pressure gradient (velocity is free in each direction, but the pressure is defined over the boundary as to respect the imposed pressure gradient) conditions on the top and bottom parts of the model to investigate their respective range of influence. The average pressure gradient and velocity for the energy dissipation on the macroscale are either found from the imposed boundary conditions or by an averaging method. To ensure robustness in our observations, each setup is analysed for three distinct random packing samples. For each of the different samples, the normalised value of the upscaled energy on micro-level is traced, following the method explained in Section 2.4. The results in Fig. 3 show that the upscaled energy for the different model setups is similar, within an error of 2%, to each other. However, upon increasing the sample size to 70%, the discharge-induced flow shows a clear upward trend in the upscaled energy, while the pressure-induced flow remains with a stable

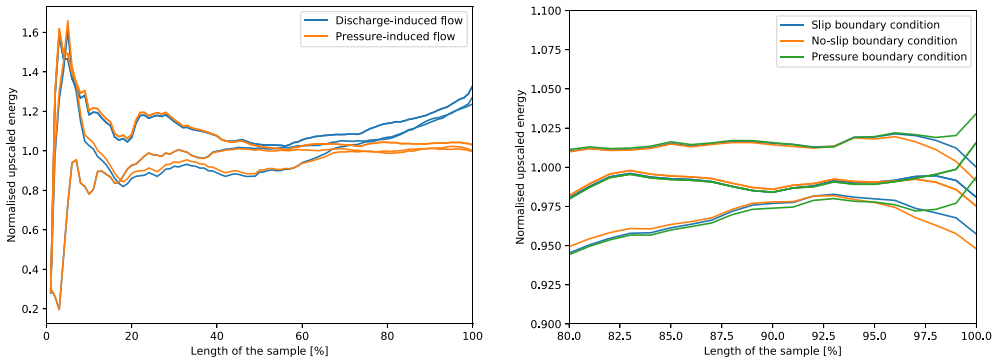

Fig. 3. The upscaled energy traced for three different random packings, using different flow model setups. On the left, the difference between the pressure- and discharge-induced flow is shown. On the right, the difference between the slip and no-slip boundary conditions is shown (implementing pressure-induced flow). We normalise the upscaled energy by the average value of all samples at 70% of the full sample size.

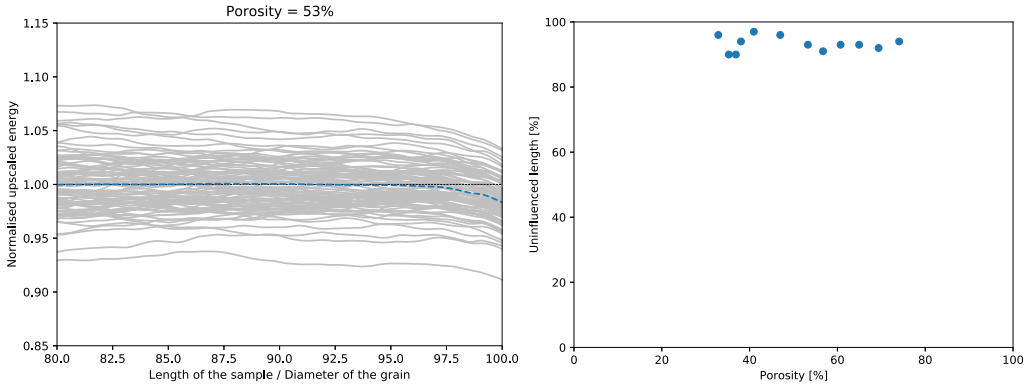

Fig. 4. The boundary effects on the normalised upscaled energy for random packing samples. An example of the evolution of the normalised energy is shown on the left for 100 samples (in grey) with a porosity of 53% and their mean in dashed blue. A divergence of the energy dissipation in the subsamples, compared to the mean, is observed in the last 5%. On the right, we report the maximum linear length without the influence of the boundary layer.

trend. At maximum size, we observe a small dip with the pressure-induced flow. Those two very characteristic boundary effects illustrate clearly that different boundary conditions result in different boundary layers. For the external slip, no-slip and pressure gradient boundary conditions, their difference only becomes discernible at the last 10% of the full sample size. Since the pressure-induced flow in combination with no-slip boundary conditions appears to be more stable, we select this setup in our contribution for the flow-through model. Note that the discharge-induced flow could yield better results with different implementations (Guibert et al., 2015), but this is out of the scope of our study.

To determine the exact size of the boundary layer, we trace 100 samples for different porosities in random packings. To emphasise the boundary effect, the average of the upscaled energy is also plotted. An example of the evolution of the energy is shown in Fig. 4 for a porosity of 53%. The upscaled energy follows the same trend for all the samples and different porosities. While the evolution of the upscaled energy has stabilised towards a certain value, once the boundary of the sample is approached a decrease is observed for each sample, which is where we assume the effect from the boundary kicks in. The exact size of the boundary layer is determined by comparing the derivative of the REV convergence with the gradient of the previously stabilised trend, at which the derivative is (close to) zero. Once the local derivative exceeds a relative error of 2%, we define it as the boundary layer. The results for each porosity are reported in Fig. 4b. We find similar sizes for other porosities, with a boundary layer between 2% to 10%. As a conservative estimate, we consider for each that the boundary layer extends to the last 10% of the sample and do our postprocessing in the remaining 90% of the samples.

3. Idealised microstructures

We mentioned in a previous section that the grain properties have a strong influence on the permeability and consequently expect those to have a direct influence on the energy dissipation. We are therefore initially considering an idealised porous medium not to let the grain shape influence the numerical results. The random packing of spheres is selected as the porous medium for this study. It represents adequately the microstructure of granular rocks but with perfect spheres instead of grains, preventing as intended any fluctuation of the permeability (Bijeljic et al., 2013).

3.1. Random packings

The distribution of the spheres in the packing is generated with the OpenMC Monte Carlo code (Romano et al., 2015). We create different sphere packings with the same characteristics by changing the seed parameter, which corresponds to a random packing set-up described in Jodrey and Tory (1985). The porosity of the microstructure is controlled by setting the packing fraction of the spheres, which is the only parameter defining the random packings since the grain diameter is fixed at 0.005 compared to a total volume of 1. Therefore, the analysis includes multiple porosities, ensuring the reliability of the results and verifying the applicability to different microstructures, all while excluding any influences of grain heterogeneities. We compute the evolution of the permeability and the energy consistency index for different porosities, increasing the packing fraction from 0.07 up to 0.62 with a step size of 0.05.

To reduce the computational cost, we take a single 2D cross-section from each generated sphere packing as our idealised microstructure.

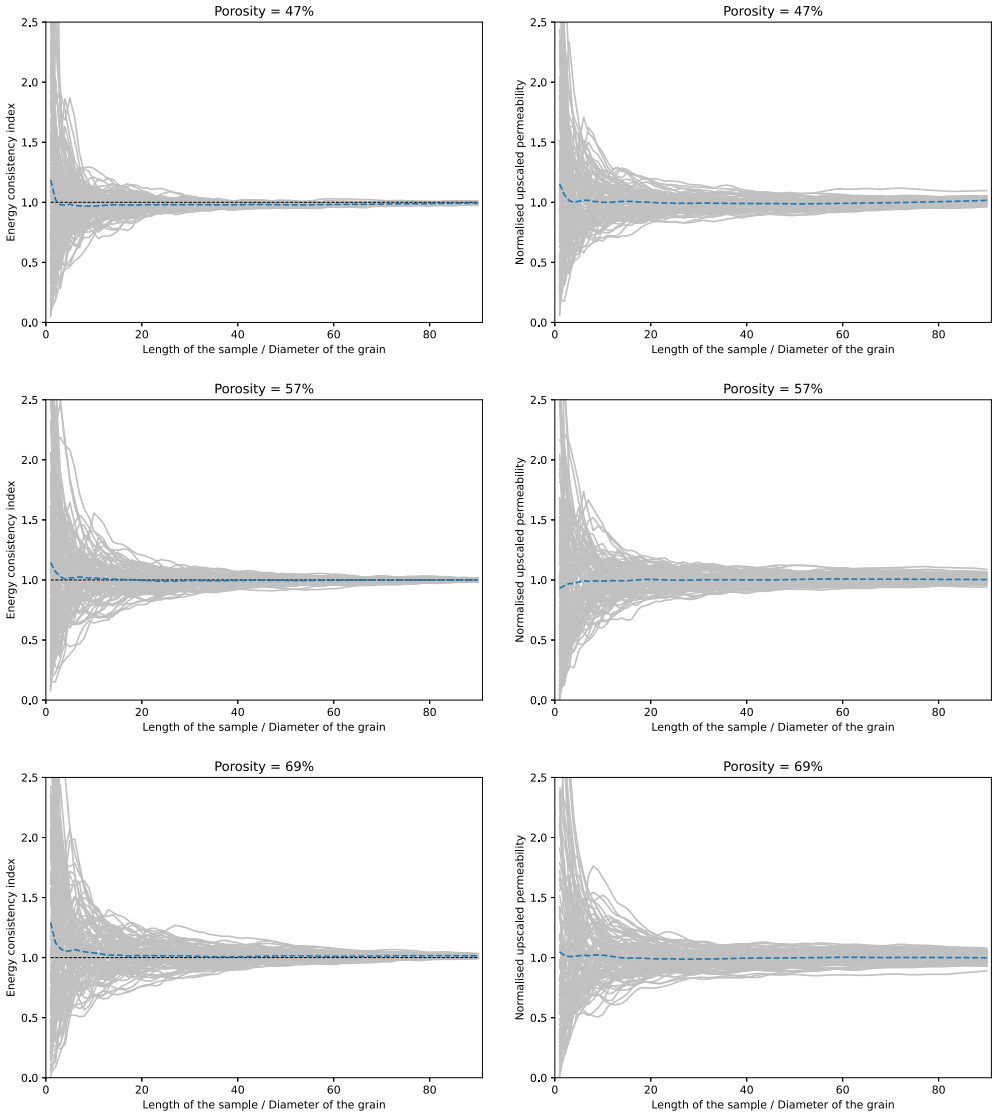

Fig. 5. REV convergence of the energy consistency index of the random packing for different porosities is presented on the left and the normalised permeability is shown on the right. Each grey line is a random packing realisation, and the blue line represents the mean of all the random packings at the considered length.

Marafini et al. (2020) demonstrated that when accounting for the third dimension, the increased flow path connectivity leads to a reduction in the size of the REV. However, the characteristics of the flow do not change. Hence, a 2D analysis remains adequate for studying the evolution of the energy consistency between different scales. Gmsh (Geuzaine and Remacle, 2009) is used to create the mesh for the cross-section, with triangular elements and a specified mesh element size.

3.2. Tracing the energy consistency index

For each porosity, 100 Monte Carlo realisations have been computed, where the REV convergence is traced for each sample with a postprocessing window growing from the middle up to the edges of the maximum subsample. The evolution of the physical properties is displayed in Fig. 5 for different porosities, where each subsample is shown in grey. To represent the overall evolution of the effective properties, the mean is plotted in blue.

The energy consistency index for each sample evolves with a unique trajectory, varying and oscillating in values, especially considering smaller volumes (observed more clearly in Fig. 4), which indicates that neither energy consistency, nor the REV is achieved at every stage of the curve. However, the mean quickly converges, which indicates at this point that the sample has reached statistical REV (Zhang et al., 2000). Indeed, the ensemble of curves outlines a cone-shaped convergence and the index variation monotonously decreases with size, which is the typical behaviour past statistical REV.

Given a reasonable level of variation of five per cent, all samples eventually display REV convergence, despite the different porosities, verifying the applicability to different micro-structural characteristics. However, we observe that the porosity of the packing affects the speed of convergence. Higher porosities display a slower convergence than lower porosities. For example, the variation of the index for the 69% porosity random packing goes lower than 0.25 at around 20 L/D and drops below 0.1 around 50 L/D. Whereas at 47% porosity, the variation falls lower than 0.25 already at 10 L/D and drops below a variation of 0.1 around 25 L/D; at 50 L/D, it is negligible.

The converged value of the mean of the energy consistency index, around which the REV convergence cone is centred, is unitary, which is our condition for energy consistency. The conclusion is that without the influence of the boundary conditions, energy consistency is only

obtained when the REV is reached. This means that the requisite of the energy conservation prescribed by the Hill–Mandel principle is only met at a certain volume, which is the REV. Current homogenisation schemes already require the REV on top of respecting the Hill–Mandel principle for valid homogenisation. Therefore, we show that we fall back to the same constraint as before. Still, one crucial advantage exists when considering the energy consistency index instead of the permeability itself to determine REV convergence: the convergence value is known to be unitary. Compared to traditional permeability REV convergence where the permeability value of the REV is unknown, we can assess instead accurately when is the REV reached and otherwise how far we are from it, as it is directly related to the distance to unitary value.

To compare the rate of REV convergence of the energy consistency index with the permeability's which is the effective property sought after, we present the results of the convergence of the corresponding normalised permeability on the right side of Fig. 5. It is evident that the overall shape of the convergence is similar. However, the traditional method exhibits slower convergence towards a specific value. At a porosity of 47% and considering 50 L/D, the variation of the energy consistency index is numerically observed to be negligible, whereas the variation of the permeability remains above 15% and similar results are observed for other porosities. The discrepancy between the two convergences can be made clear when understanding that the ratio of the energies of the different scales needs to become equal before their values converge, at which point the permeability will converge equivalently. On a practical level though, we can consider the convergence to happen realistically around the same timing but with a variation that could be bigger for the permeability.

4. Application to real microstructures

Using the random packing of spheres, we showed that energy consistency is found intrinsically at REV. In this section, we consider real rock microstructures to verify whether this result still holds despite the influence of the natural heterogeneities from the rock.

The process of digital rock reconstruction follows the framework of Lesueur et al. (2017). Segmented 2D microCT-scans are translated to 3D computational models, in which the rock and void space are separated. In order to reduce the computational costs of the simulations, we use the Displaced Boundary Method (Lesueur et al., 2022b) to conform the pore–boundary interface to a coarser background mesh. It is shown that mesh convergence is still achieved with a coarser mesh, which results in the reduction of computational costs of the simulations. Those mesh structures are used to run the Stokes flow simulations, with a similar model set up as described in Section 2, except in 3D. Because of large run times, the simulations are performed using the DelftBlue supercomputer (Delft High Performance Computing Centre (DHPC)).

While an unlimited number of perfect random packings can be generated by the algorithm, the microstructures obtained from μCT-scanning are limited by the sample size and scan resolution. Tracing the energy consistency index through the full sample provides a single curve and therefore is not statistically representative. To obtain some information about the variation of the energy consistency during the REV convergence, the sample is divided into multiple subsamples. The size of the subsamples is selected bigger than the average grain size to ensure the behaviour of the fluid transport inside the rock is accurately represented. The sample is divided into $4^3 = 64$ equal-sized subsamples. Splitting it into fewer subsamples would result in a bigger subsample size, yet less statistical representativeness. Splitting it into more subsamples would result in a tiny maximum size of the samples which might not be representative. The subsamples do not overlap in order to ensure the independence of the results. For each subsample, the energy consistency index is traced away from the boundary layer, growing in size from the centre up to the edges.

4.1. LV60A sandpack

The first microstructure is the LV60A sandpack (Imperial College Consortium On Pore-Scale Modelling, 2014b), shown in Fig. 6a. Sandpacks are monomineralic, which makes them quite homogeneous in both grain size and shape, yet they include natural heterogeneities such as the grain roughness and non-sphericity of the grains. Sandpacks have high permeability, as the voids within the sample are connected throughout. The influence of the occurring natural heterogeneities on the energy consistency is expected to be low, considering the fairly homogeneous characteristics of the sandpack. Therefore, this rock is most suitable to start verifying the result obtained on the random packings. The LV60A sandpack has a full size of just above three mm. With a scan resolution of $10.008\ \mu m$, the full sample contains 300^3 voxels.

Despite the lack of statistical representativeness, the full sample displays undoubtedly convergence of REV where the energy consistency index remains stable at the converged value indefinitely. The ensemble of grey lines conveys more information. The cone of convergence appears once again. The initial variation is larger than for the random packing which prompts us to rescale the y-axis twice larger. We observe this time a non-negligible amount of subsamples that are non-percolating, distinguished by an energy consistency index of 0. Those cases did not appear in the random packings. As expected, the mean converges faster than the single curve of the full sample and the convergence is reached quickly, before the maximum size of the subsamples. While the maximum sample size is a bit restrictive, we expect the level of variation to be close to convergence. This is confirmed in the study of Mostaghimi et al. (2012), which finds a REV of 1.1 mm in linear length. The mean value of the energy consistency index as well as the converged value for the full sample is unitary, within a small margin of 0.08, indicating energy consistency at REV as it was shown for the random packing of spheres.

4.2. S1 sandstone

The second sample is the S1 sandstone (Imperial College Consortium On Pore-Scale Modelling, 2014c), shown in Fig. 7a. Whereas sandpacks are typically made of individual grains, sandstone is a rock with a much more cohesive structure where the grains are cemented together by minerals. Due to this cement fraction, sandstones often have a lower permeability than sandpacks, as the voids show a lower connectivity and flow paths are more tortuous. This cementation overall results in slightly more heterogeneous properties. With a scan resolution of $8.7\ \mu m$ for a total sample length of 2.6 mm, the S1 sandstone sample is reconstructed with 300^3 voxels.

The results of the S1 sandstone are plotted in Fig. 7b. The curve of the full sample differs from the sandpack, strong variations stabilise past 0.6 mm of size, yet a completely stable line, which was observed with the sandpack, is not observed numerically. The energy consistency index tracing ends with a value of 0.91. As expected, the values of the energy consistency index are more scattered within the subsamples of the sandstone, as shown in grey. The index displays values ranging from zero up to five in subsamples of size 0.4 mm. To put it into contrast, this region was only half as big when the sandpack was analysed. From 0.25 mm, the index exhibits a cone-shaped convergence towards a value of one, like the sandpack and random packings. Although, at the maximum size of the subsamples (0.54 mm), the index still varies by an amplitude of 0.6. Looking at the mean, we accordingly have large variations before the cone of convergence can be observed. We then observe light oscillation around the unitary value. Convergence seems not to be observed yet. Nonetheless, with the mean value near one along with the decreasing variation of the index, it is logical to assume we are close to the REV size along with energy consistency. Similar trends are shown by Mostaghimi et al. (2012) who traced the REV convergence of the permeability of this sandstone. The variation of the permeability dampens out, but the average permeability of the full sample still presents the same decreasing trend we observed when the full sample of the sandstone is considered.

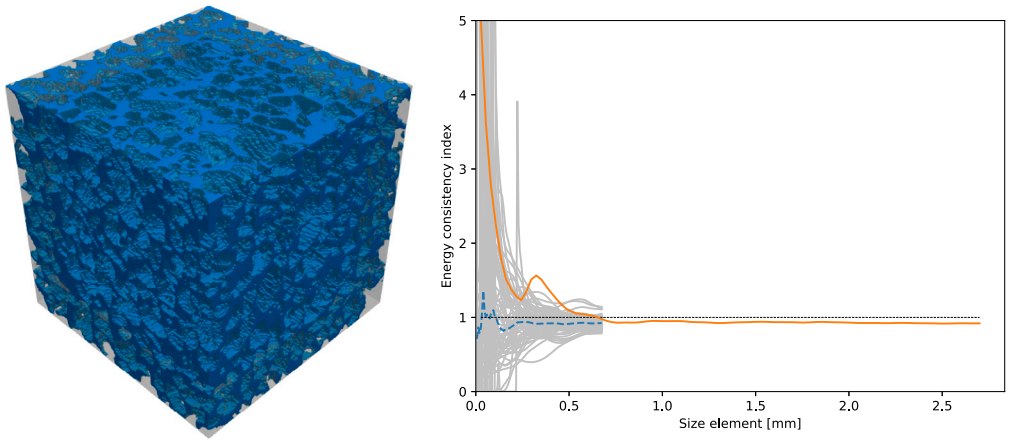

Fig. 6. On the left a reconstruction of the LV60A sandpack pore space is displayed. On the right, the tracing of the energy consistency index of the sandpack is shown. The upscaled energy of the 64 subvolumes is shown with grey lines and the average of the upscaled energy is shown with the blue dashed line. The index for the full sample is shown in orange.

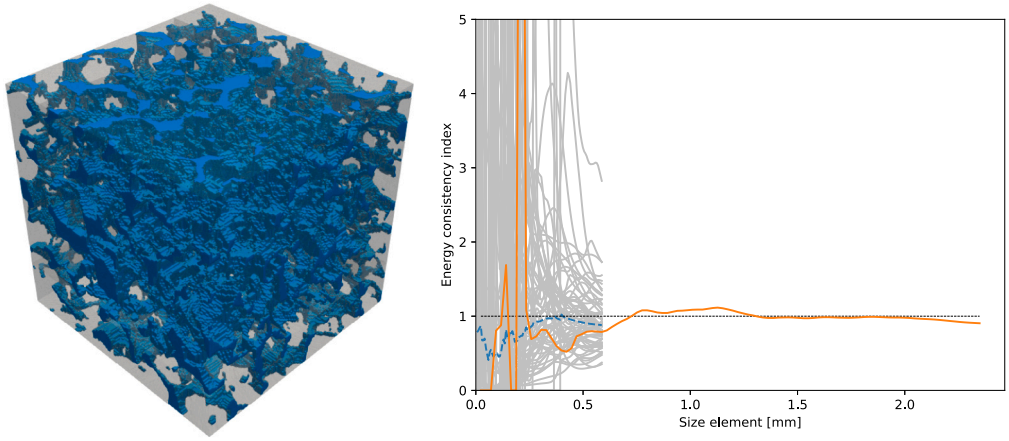

Fig. 7. On the left a reconstruction of the S1 sandstone pore space is displayed. On the right, the tracing of the energy consistency index of the sandstone is shown. The upscaled energy of the 64 subvolumes is shown with grey lines and the average of the upscaled energy is shown with the blue dashed line. The index for the full sample is shown in orange.

4.3. Ketton limestone

The third sample is the Ketton limestone (Imperial College Consortium On Pore-Scale Modelling, 2015), shown in Fig. 8a. Limestone is mainly composed of calcium carbonate and therefore usually quite heterogeneous. The grain shape and sizes vary substantially and the pore spaces may not always be connected. This Ketton sample is rather homogeneous for a limestone and has voids reasonably well connected. Where many similar rocks do not reach easily the REV size, we expect this to be different with the Ketton rock sample. The sample with a size of just over 3 mm has a much higher CT-scan image resolution compared to the others, of 3 μm, resulting in a digitised microstructure with 1000^3 voxels.

The results for the Ketton are plotted in Fig. 8b. The variation of the energy consistency index displays a similar trend to the sandstone. Despite a large variation initially, the cone of convergence eventually appears. We find a more stable mean than the sandstone. However, the value seems to be below one, with an exact value of 0.94, close to one. The full sample reaches a stable value of the energy consistency index of one after 1.75 mm in length. All those results indicate that energy consistency along with the REV should be numerically determined naturally between 1 to 2 mm.

4.4. C2 carbonate

The last sample is the C2 carbonate (Imperial College Consortium On Pore-Scale Modelling, 2014a), shown in Fig. 9a. The C2 carbonate exhibits a high heterogeneity in grain properties and a low connectivity of the voids, which results in a low permeability overall. Mostaghimi et al. (2012) has shown that the size of the REV is not observed numerically for the permeability, even when the full sample is taken into account. This sample is the most heterogeneous considered in this study. The sample has an image resolution of 5.7 μm and with the total size of the sample of 2.3 mm, the result is 400^3 voxels.

The results for the C2 carbonate are shown in Fig. 9b. The subsamples show an unparallelled variation of the energy consistency index, compared to the previously assessed rock samples. Whereas we find values of the index from zero and above five until 0.4 mm in the Ketton and S1, the C2 exhibits these values still up to 0.5 mm, which is the maximum size of the subsamples considered. The average value of the energy consistency index of the subsamples, shown in blue, oscillates until the end and is not close to converging to one. The energy consistency index from the full sample, plotted in orange, appears to be more stable towards full size but noticeably below one (0.67). Eventually, not

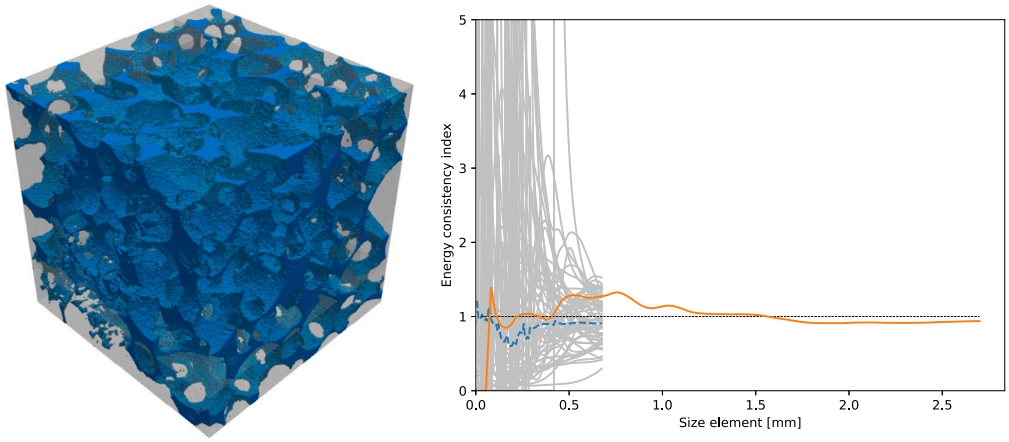

Fig. 8. On the left a reconstruction of the Ketton limestone pore space is displayed. On the right, the tracing of the energy consistency index of the limestone is shown. The upscaled energy of the 64 subvolumes is shown with grey lines and the average of the upscaled energy is shown with the blue dashed line. The index for the full sample is shown in orange.

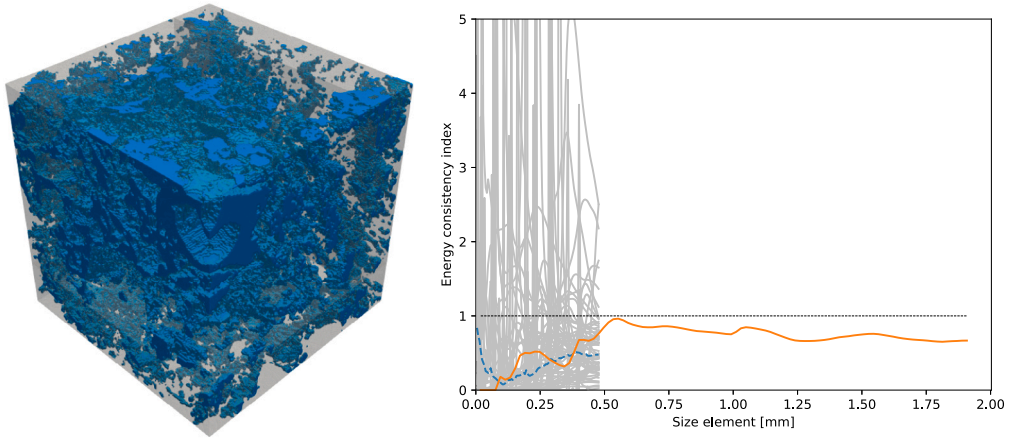

Fig. 9. On the left a reconstruction of the C2 carbonate pore space is displayed. On the right, the tracing of the energy consistency index of the carbonate is shown. The upscaled energy of the 64 subvolumes is shown with grey lines and the average of the upscaled energy is shown with the blue dashed line. The index for the full sample is shown in orange.

only do we not observe REV convergence from all this variation, we also have little confidence in providing any prediction on the expected size of REV. The conclusion is that energy consistency cannot be numerically determined for the C2 carbonate and valid homogenisation cannot be applied. The previously assessed rock samples show a clear trend of convergence after the percolation threshold has been reached. As we still observe subsamples that are below the percolation threshold for the C2 carbonate at the maximum size considered, it is coherent with our previous results that convergence is not observed.

5. Conclusion

In this contribution, the traditional ways to apply Hill–Mandel principle of energy conservation throughout the transition of scales in homogenisation methods were revisited. This requirement for rigorous homogenisation is usually enforced by applying specific boundary conditions, which however influences the resulting effective properties, in both magnitude and rotation for permeability. The necessity of those boundary conditions was investigated and we observed that Hill–Mandel principle could be respected independently from the boundary conditions used.

Using the results of Stokes-flow simulations through digitised microstructures, this study assessed the energy consistency of fluid transport inside idealised and real microstructures inside an intrinsic volume, away from the boundary layer and therefore uninfluenced by the boundary conditions. We numerically observed that energy consistency is linked to reaching the Representative Elementary Volume (REV). When this size is reached, all requisites are met for rigorous homogenisation to be applied. And from Thovert and Mourzenko (2020), we know that the effective property computed at this size in an intrinsic volume will be exact, instead of an upper or lower bound estimation due to the use of specific boundary conditions. It is important to note that the result obtained should be extendable to other properties of interest and for different physics since the Hill–Mandel principle is universal. Taking the example of solid mechanics for example, the difference will be that the energy dissipation will be defined as the product of the strain rate and the stress.

In this study, we introduced an index for energy consistency which is the ratio between the micro- to macro-scale energy of the fluid transport. This index follows a typical REV convergence in a cone shape. However, the difference and advantage of using that index during a REV convergence is that – from the results of this study – we know that the index will converge to one at REV, whereas traditional homogenisation schemes use an iterative process to determine the stabilised property value, which is usually unknown. This index becomes therefore a great indicator of REV which can also easily indicate as supplementary information the error we have from REV.

We extended the numerical results of the random packings to real rock microstructures, which include natural heterogeneities. We show

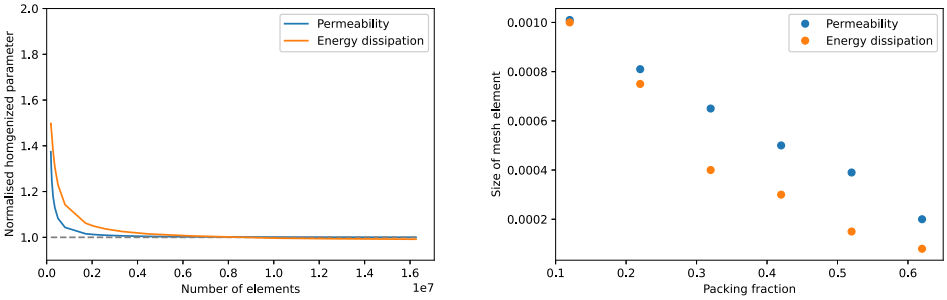

Fig. A.10. The mesh convergence of the homogenised properties inside a 2D cross-section of a random packing, normalised to their respective final value, for a porosity of 53% (left). On the right, we show the evolution of the mesh size needed for mesh convergence with porosity.

that those heterogeneities mainly influence the width of the base of the cone of convergence, as the variation at the base is a lot higher than for the random packings. Still, the cone converges towards an energy consistency index of one, which means the Hill–Mandel principle is eventually respected. Despite a slower convergence, the heterogeneities of natural rocks do not influence the principle of energy conservation and it remains possible to apply valid homogenisation at REV, even when heterogeneities are present.

We note that the size past which the REV convergence cone can be found inside real microstructures seems to directly depend on the percolation threshold. The energy consistency index fluctuates considerably when sub-samples are not percolating. This is observed on highly heterogeneous samples and this behaviour prevents an accurate prediction of REV. In comparison, when the percolation threshold is reached, the mean value of the energy consistency index stabilises and reaches convergence quickly.

CRediT authorship contribution statement

Sijmen Zwarts: Conceptualization, Investigation, Software, Writing – original draft, Writing – review & editing. **Martin Lesueur:** Conceptualization, Software, Supervision, Writing – original draft, Writing – review & editing.

Declaration of competing interest

The authors declare that they have no known competing financial interests or personal relationships that could have appeared to influence the work reported in this paper.

Data availability

Data will be made available on request.

Appendix A. Mesh convergence

Mesh convergence is a crucial aspect of numerical simulations, as it ensures that the solution obtained is independent of the discretisation used and thus can be considered to be numerically accurate. As we increase homogeneously the number of mesh elements, we find that both the energy consistency index and the permeability converge towards a respective unique value, see Fig. A.10. We consider the mesh to be converged when we fall below a 2% error of the normalised value. The mesh convergence is obtained at different mesh resolutions for different porosities (see Table A.1). This difference is due to the particular attention to meshing that is required at the boundary of the spheres. Those circles of the cross-section are challenging to represent using a triangular mesh configuration, which results in the need for more elements at the boundary compared to the pore space in between the circles. Consequently, higher porosities, which include more circles, require a smaller mesh element size for mesh convergence. Note that the mesh convergence for the permeability is found earlier than for the energy. While the permeability is computed via Darcy's law, the energy is postprocessed on the micro level, which means that both the velocity of the fluid and the pressure need to reach mesh convergence and the accumulation of error, therefore, leads to a slower mesh convergence.

Table A.1
Element sizes for mesh convergence of the different samples.

Porosity	Mesh element size
74%–61%	0.0004
61%–57%	0.0004
57%–38%	0.0001
38%–35%	0.00009
35%–32%	0.00008

Appendix B. Model verification

The Kozeny–Carman equation (Kozeny, 1927; Carman, 1937) is a relation commonly employed to find the permeability of porous media. The relationship was originally developed by Kozeny using the simplified model of parallel capillary tubes of equal length and diameter to describe a packed bed. Carman later calibrated the equation experimentally on real samples. The model assumes that the spheres have a uniform diameter and do not overlap. The flow of the fluid is assumed to be governed by Darcy's law, as the flow is laminar. The pores between the spheres are assumed narrow and any permeability of the solid grains is neglected. As these assumptions match our model rather well, the equation is used to validate our model.

The Kozeny–Carman model relates permeability in the direction of the flow (k) with the sphericity of the particles in the packed bed (ϕ_s), the porosity of the sample, the average diameter of the grains (D_p) and the Kozeny constant (K), depending on the tortuosity of the sample:

$$k = \phi_s^2 \frac{\varphi^3 D_p^2}{36K(1-\varphi)^2} \tag{B.1}$$

The results of the permeability computed from the random packing cross-section and Kozeny–Carman model are compared and shown in Fig. B.11. The evolution of permeability with porosity is similar in trend. However, we encounter the same limitation as noted by Marafini et al. (2020), which demonstrated that the exact values obtained from two-dimensional models differ from those derived through post-processing of three-dimensional models. Despite this discrepancy, the observed trend remains consistent. Considering the similarity between our setup and that of Lesueur et al. (2017), we conclude that our model setup is correct.

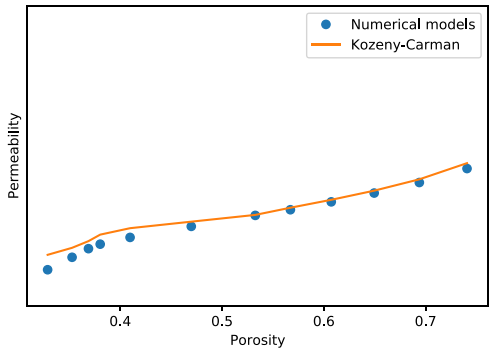

Fig. B.11. Comparison of permeability from different porosities, computed with the Kozeny–Carman (orange) and the numerical models (blue).

References

Andrae, H., Combaret, N., Dvorkin, J., Glatt, E., Han, J., Kabel, M., Keehm, Y., Krzikalla, F., Lee, M., Madonna, C., Marsh, M., Mukerji, T., Saenger, E.H., Sain, R., Saxena, N., Ricker, S., Wiegmann, A., Zhan, X., 2013. Digital rock physics benchmarks—part II: Computing effective properties. Comput. Geosci. 50, 33–43. http://dx.doi.org/10.1016/j.cageo.2012.09.008.

Auriault, J.-L., 2011. Heterogeneous periodic and random media. Are the equivalent macroscopic descriptions similar? Internat. J. Engrg. Sci. 49 (8), 806–808. http://dx.doi.org/10.1016/j.ijengsci.2011.01.005.

Beard, D.C., Weyl, P.K., 1973. Influence of texture on porosity and permeability of unconsolidated sand. AAPG Bull. 57, http://dx.doi.org/10.1306/819a4272-16c5-11d7-8645000102c1865d.

Bijeljic, B., Raeini, A., Mostaghimi, P., Blunt, M.J., 2013. Predictions of non-Fickian solute transport in different classes of porous media using direct simulation on pore-scale images. Phys. Rev. E 87 (1), 013011. http://dx.doi.org/10.1103/physreve.87.013011.

Bøe, O., 1994. Analysis of an upscaling method based on conservation of dissipation. Transp. Porous Media 17 (1), 77–86. http://dx.doi.org/10.1007/bf00624051.

Carman, P.C., 1937. Fluid flow through granular beds. Trans. Inst. Chem. Eng. 15, 150–166.

Cox, M.R., Budhu, M., 2008. A practical approach to grain shape quantification. Eng. Geol. 96 (1–2), 1–16. http://dx.doi.org/10.1016/j.enggeo.2007.05.005.

Darcy, H.P.G., 1856. Dètermination des lois d'ècoulement de l'eau à travers le sable.

Delft High Performance Computing Centre (DHPC), 2022. DelftBlue supercomputer (phase 1). https://www.tudelft.nl/dhpc/ark:/44463/DelftBluePhase1.

Du, X., Ostoja-Starzewski, M., 2006. On the size of representative volume element for Darcy law in random media. Proc. R. Soc. A 462 (2074), 2949–2963. http://dx.doi.org/10.1098/rspa.2006.1704.

Gerke, K.M., Karsanina, M.V., Katsman, R., 2019. Calculation of tensorial flow properties on pore level: Exploring the influence of boundary conditions on the permeability of three-dimensional stochastic reconstructions. Phys. Rev. E 100 (5), 053312. http://dx.doi.org/10.1103/physreve.100.053312.

Geuzaine, C., Remacle, J.-F., 2009. Gmsh: A 3-D finite element mesh generator with built-in pre- and post-processing facilities. Internat. J. Numer. Methods Engrg. 79 (11), 1309–1331. http://dx.doi.org/10.1002/nme.2579.

Guibert, R., Horgue, P., Debenest, G., Quintard, M., 2015. A comparison of various methods for the numerical evaluation of porous media permeability tensors from pore-scale geometry. Math. Geosci. 48 (3), 329–347. http://dx.doi.org/10.1007/s11004-015-9587-9.

Hill, R., 1963. Elastic properties of reinforced solids: Some theoretical principles. J. Mech. Phys. Solids 11 (5), 357–372. http://dx.doi.org/10.1016/0022-5096(63)90036-x.

Imperial College Consortium On Pore-Scale Modelling, 2014a. C2 Carbonate. Figshare, http://dx.doi.org/10.6084/m9.figshare.1189258.

Imperial College Consortium On Pore-Scale Modelling, 2014b. LV60A Sandpack. Figshare, http://dx.doi.org/10.6084/M9.FIGSHARE.1153795.

Imperial College Consortium On Pore-Scale Modelling, 2014c. S1 Sandstone. Figshare, http://dx.doi.org/10.6084/M9.FIGSHARE.1189274.V1.

Imperial College Consortium On Pore-Scale Modelling, 2015. Ketton Limestone. Figshare, https://imperialcollegelondon.app.box.com/v/iccpsim-ketton2015.

Jänicke, R., Quintal, B., Steeb, H., 2015. Numerical homogenization of mesoscopic loss in poroelastic media. Eur. J. Mech. A Solids 49, 382–395.

Jodrey, W.S., Tory, E.M., 1985. Computer simulation of close random packing of equal spheres. Phys. Rev. A 32 (4), 2347.

Kanit, T., Forest, S., Galliet, I., Mounoury, V., Jeulin, D., 2003. Determination of the size of the representative volume element for random composites: statistical and numerical approach. Int. J. Solids Struct. 40 (13–14), 3647–3679. http://dx.doi.org/10.1016/s0020-7683(03)00143-4.

Khoei, A., Hajiabadi, M., 2018. Fully coupled hydromechanical multiscale model with microdynamic effects. Internat. J. Numer. Methods Engrg. 115 (3), 293–327. http://dx.doi.org/10.1002/nme.5805.

Khoei, A.R., Saeedmonir, S., Bonabi, A.M., 2023. Computational homogenization of fully coupled hydro-mechanical analysis of micro-fractured porous media. Comput. Geotech. 154, 105121.

Kozeny, J., 1927. Uber Kapillare Leitung Der Wasser in Boden, Vol. 136. Royal Academy of Science, Vienna, pp. 271–306, Proc. Class I.

Larsson, F., Runesson, K., Saroukhani, S., Vafadari, R., 2011. Computational homogenization based on a weak format of micro-periodicity for RVE-problems. Comput. Methods Appl. Mech. Engrg. 200 (1), 11–26. http://dx.doi.org/10.1016/j.cma.2010.06.023, URL: https://www.sciencedirect.com/science/article/pii/S0045782510001908.

Lesueur, M., Casadiego, M.C., Veveakis, M., Poulet, T., 2017. Modelling fluid-microstructure interaction on elasto-visco-plastic digital rocks. Geomech. Energy Environ. 12, 1–13. http://dx.doi.org/10.1016/j.gete.2017.08.001.

Lesueur, M., Guével, A., Poulet, T., 2022a. Reconciling asymmetry observations in the permeability tensor of digital rocks with symmetry expectations. Adv. Water Resour. 170, 104334. http://dx.doi.org/10.1016/j.advwatres.2022.104334.

Lesueur, M., Rattez, H., Colomes, O., 2022b. MicroCT scans permeability computation with an unfitted boundary method to improve coarsening accuracy. Comput. Geosci. 166, 105118. http://dx.doi.org/10.1016/j.cageo.2022.105118.

Mandel, J., 1972. Plasticité Classique Et Viscoplasticité: Course Held at the Department of Mechanics of Solids. Courses and Lectures - International Centre for Mechanical Sciences Springer-Verlag, New York, NY, 1972.

Marafini, E., Rocca, M.L., Fiori, A., Battiato, I., Prestininzi, P., 2020. Suitability of 2D modelling to evaluate flow properties in 3D porous media. Transp. Porous Media 134 (2), 315–329. http://dx.doi.org/10.1007/s11242-020-01447-4.

Marinelli, F., Van den Eijnden, A., Sieffert, Y., Chambon, R., Collin, F., 2016. Modeling of granular solids with computational homogenization: Comparison with Biot's theory. Finite Elem. Anal. Des. 119, 45–62.

Mostaghimi, P., Blunt, M.J., Bijeljic, B., 2012. Computations of absolute permeability on micro-CT images. Math. Geosci. 45 (1), 103–125. http://dx.doi.org/10.1007/s11004-012-9431-4.

Nguyen, V.-D., Béchet, E., Geuzaine, C., Noels, L., 2012. Imposing periodic boundary condition on arbitrary meshes by polynomial interpolation. Comput. Mater. Sci. 55, 390–406. http://dx.doi.org/10.1016/j.commatsci.2011.10.017.

Paéz-García, C.T., Valdés-Parada, F.J., Lasseux, D., 2017. Macroscopic momentum and mechanical energy equations for incompressible single-phase flow in porous media. Phys. Rev. E 95 (2), 023101. http://dx.doi.org/10.1103/physreve.95.023101.

Permann, C.J., Gaston, D.R., Andrš, D., Carlsen, R.W., Kong, F., Lindsay, A.D., Miller, J.M., Peterson, J.W., Slaughter, A.E., Stogner, R.H., Martineau, R.C., 2020. MOOSE: Enabling massively parallel multiphysics simulation. SoftwareX 11, 100430. http://dx.doi.org/10.1016/j.softx.2020.100430, URL: http://www.sciencedirect.com/science/article/pii/S2352711019302973.

Peterson, J.W., Lindsay, A.D., Kong, F., 2018. Overview of the incompressible Navier–Stokes simulation capabilities in the MOOSE framework. Adv. Eng. Softw. 119, 68–92. http://dx.doi.org/10.1016/j.advengsoft.2018.02.004.

Pouya, A., Fouche, O., 2009. Permeability of 3D discontinuity networks: New tensors from boundary-conditioned homogenisation. Adv. Water Resour. 32 (3), 303–314. http://dx.doi.org/10.1016/j.advwatres.2008.08.004.

Renard, P., de Marsily, G., 1997. Calculating equivalent permeability: a review. Adv. Water Resour. 20 (5–6), 253–278. http://dx.doi.org/10.1016/s0309-1708(96)00050-4.

Romano, P.K., Horelik, N.E., Herman, B.R., Nelson, A.G., Forget, B., Smith, K., 2015. OpenMC: A state-of-the-art Monte Carlo code for research and development. Ann. Nucl. Energy 82, 90–97. http://dx.doi.org/10.1016/j.anucene.2014.07.048.

Saeedmonir, S., Khoei, A.R., 2022. Multiscale modeling of coupled thermo-hydro-mechanical analysis of heterogeneous porous media. Comput. Methods Appl. Mech. Engrg. 391, 114518. http://dx.doi.org/10.1016/j.cma.2021.114518.

Sandström, C., Larsson, F., Runesson, K., 2016. Homogenization of coupled flow and deformation in a porous material. Comput. Methods Appl. Mech. Engrg. 308, 535–551.

Shi, J., Boyer, G., Mourzenko, V.V., Thovert, J.-F., 2020. On the influence of boundary conditions when determining transport coefficients from finite samples of porous media: Assessment for tomographic images of real materials. Transp. Porous Media 132 (3), 561–590. http://dx.doi.org/10.1007/s11242-020-01404-1.

Su, F., Larsson, F., Runesson, K., 2011. Computational homogenization of coupled consolidation problems in micro-heterogeneous porous media. Internat. J. Numer. Methods Engrg. 88 (11), 1198–1218. http://dx.doi.org/10.1002/nme.3221.

Terada, K., Hori, M., Kyoya, T., Kikuchi, N., 2000. Simulation of the multi-scale convergence in computational homogenization approaches. Int. J. Solids Struct. 37 (16), 2285–2311. http://dx.doi.org/10.1016/S0020-7683(98)00341-2, URL: https://www.sciencedirect.com/science/article/pii/S0020768398003412.

Thovert, J.-F., Mourzenko, V.V., 2020. On the influence of boundary conditions when determining transport coefficients from digital images of heterogeneous media. Adv. Water Resour. 141, 103612. http://dx.doi.org/10.1016/j.advwatres.2020.103612.

Torskaya, T., Shabro, V., Torres-Verdín, C., Salazar-Tio, R., Revil, A., 2014. Grain shape effects on permeability, formation factor, and capillary pressure from pore-scale modeling. Transp. Porous Media 102 (1), 71–90. http://dx.doi.org/10.1007/s11242-013-0262-7.

Whitaker, S., 1986. Flow in porous media I: A theoretical derivation of Darcy's law. Transp. Porous Media 1 (1), 3–25. http://dx.doi.org/10.1007/bf01036523.

Zakirov, T., Khramchenkov, M., 2022. Study of the pore space heterogeneity effect on the absolute permeability tensors calculated under different boundary conditions and driving forces using a "Computational Rock Physics" technology. J. Pet. Sci. Eng. 216, 110750. http://dx.doi.org/10.1016/j.petrol.2022.110750.

Zhang, D., Zhang, R., Chen, S., Soll, W.E., 2000. Pore scale study of flow in porous media: Scale dependency, REV, and statistical REV. Geophys. Res. Lett. 27 (8), 1195–1198. http://dx.doi.org/10.1029/1999gl011101.